478 *Biochemistry* **2010,** *49,* 478–486
DOI: 10.1021/bi9016236

BIOCHEMISTRY
including biophysical chemistry & molecular biology
Article

Nuclear Magnetic Resonance Secondary Shifts of a Light-Harvesting 2 Complex Reveal Local Backbone Perturbations Induced by Its Higher-Order Interactions†

Anjali Pandit,* Piotr K. Wawrzyniak, Adriaan J. van Gammeren,‡ Francesco Buda, Swapna Ganapathy, and Huub J. M. de Groot

Leiden Institute of Chemistry, Leiden University, P.O. Box 9502, 2300 RA Leiden, The Netherlands. ‡Present address: Klinisch Chemisch en Hematologisch Laboratorium, Amphia Ziekenhuis, Langendijk 75, 4819 EV Breda, The Netherlands.

Received September 16, 2009; Revised Manuscript Received November 26, 2009

ABSTRACT: Protein nuclear magnetic resonance (NMR) secondary chemical shifts are widely used to predict the secondary structure, and in solid-state NMR, they are often the only unambiguous structural parameters available. However, the employed prediction methods are empirical in nature, relying on the assumption that secondary shifts are only affected by shielding effects of neighboring atoms. We analyzed the secondary shifts of a photosynthetic membrane protein with a high density of chromophores and very tight packing, the light-harvesting 2 (LH2) complex of *Rhodopseudomonas acidophila*. A relation was found between secondary shift anomalies and protein−protein or pigment−protein tertiary and quaternary contacts. For several residues, including the bacteriochlorophyll-coordinating histidines (αH31 and *β*H30) and the phenylalanine αF41 that has strongly twisted C_b-C_a-C and C_a-C-N conformations in the LH2 crystal structure, the perturbing effects on the backbone chemical shifts were tested by density functional theory (DFT) calculations. We propose that higher-order interactions in the tightly packed complex can induce localized perturbations of the backbone conformation and electronic structure, related to functional pigment−protein or protein−protein interactions.

In solution NMR[1] investigations and in solid-state NMR of structurally relaxed proteins, displacements of secondary chemical shifts in proteins derive mainly from local shielding effects that depend on bond lengths and torsion angles, which correlate with the secondary structure (*1*, *2*). While for soluble proteins abundant $^1H-^1H$ distance restraints are obtained from multidimensional nuclear Overhauser enhancement (NOE) spectra, for proteins in the solid state the chemical shifts are often the only unambiguous NMR structural parameters available. By comparison of secondary chemical shifts with reference databases of protein NMR structures, dihedral angles can be estimated, and protein sequences are classified as *β*-sheet, α-helical, or coil-type. However, these methods are empirical and inherently biased to predict the most commonly found secondary structure motifs in proteins, based on the assumption that secondary chemical shifts are markers for the local structure around a nucleus that are sensitive to the $^{13}C-N$ bond lengths and the $N-C_a-C$ torsion angles. In addition to the isotropic chemical shifts, information about the backbone folding and local environment can be obtained from the $^{13}C-^{15}N$ distances (*3*) and from the spinning sideband intensities (*4*). Chemical shift anisotropy (CSA) tensors for the amide and carbonyl resonances of microcrystalline proteins have been determined by high-resolution solid-state NMR (*5*, *6*). Furthermore, it has been shown that $^1H-^1H$ spin diffusion experiments can detect through-space long-range distance correlations (*7*). Structure validation can be performed starting from molecular models by summing classically calculable shift contributions for the nuclei, random coil, electrostatic, ring current, and hydrogen bond factors (*8*). In this way, the sensitivity of the secondary shifts to different local and long-range parameters has been determined experimentally and computationally, and these empirical methods have been applied in solid-state NMR structural studies as well (*9*, *10*). A number of studies have been devoted to improving protein structure prediction by NMR, including the combination of empirical chemical shift prediction and structure optimization procedures with Monte Carlo protein fragment assembly (*11*), or by comparing experimental $^{13}C_a$ chemical shifts to computed $^{13}C_a$ shifts from quantum chemical calculations (*12*).

In this paper, we analyze the solid-state secondary shifts of the light-harvesting 2 (LH2) antenna complex of the purple bacterium *Rhodopseudomonas acidophila*, an oligomeric membrane protein with a 9-fold symmetry that is densely packed with cofactors, and look for the origin of its pronounced secondary shift anomalies. For the LH2 complex, a sequence-specific chemical shift assignment has been obtained (*13*, *14*), but the secondary structure of the LH2 *Rps. acidophila* polypeptides could not be predicted from the residual assignments using TALOS that generates dihedral angles

†A.P. was supported by VENI Grant 700.55.408 from The Netherlands Organization of Scientific Research. We acknowledge the support from the Stichting Nationale Computerfaciliteiten (NCF-NWO) for the use of the SARA supercomputer facilities.

*To whom correspondence should be addressed: Leiden Institute of Chemistry, Department of Solid-State NMR, Leiden University, P.O. Box 9502, 2300 RA Leiden, The Netherlands. E-mail: a.pandit@chem.leidenuniv.nl. Phone: +31 (0)71-5275271. Fax: +31(0)71-5274603.

[1]Abbreviations: NMR, nuclear magnetic resonance; LH2, light-harvesting 2; DFT, density functional theory; BChl, bacteriochlorophyll; Car, carotenoid; MAS, magic angle spinning; TMS, tetramethylsilane; PDB, Protein Data Bank; rms, root-mean-square; BMRB, Biological Magnetic Resonance Bank; BLYP, Becke−Lee−Yang−Parr; ADF, Amsterdam functional theory; TZP, triple zeta polarized.

 Published on Web 12/02/2009

based on NMR backbone chemical shifts (*14*, *15*). The LH2 antenna complex is involved in the first step of photosynthesis, in which sunlight is captured, followed by transfer of excitation energy to the LH1 core complexes that surround the photosynthetic reaction centers (*16*). The special features of the purple bacterial antenna systems, i.e., their robustness, the high ring-shaped symmetry of repeating subunits, and the possibility for self-assembly in vitro (*17*−*19*), make them of particular interest as templates for construction of hybrid biomimetic devices (*20*, *21*). For the LH2 complex of *Rps. acidophila*, the crystal structure has been determined at 2.0 Å (*22*), presenting a nonamer ring of identical $\alpha\beta$ polypeptide dimer subunits that each comprise three bacteriochlorophylls (BChls) and one carotenoid (Car). Two BChls are sandwiched between the α and β polypeptide and oriented perpendicular to the membrane plane. Together, they form rings of BChl dimers, called the B850 band, since they have a red-shifted Q_y absorption band around 850 nm. Efficient energy transfer occurs among the B850 BChls through excitonic interactions that are responsible for the major part of the red shift (*23*). The third BChl species collectively form the B800 band, with a Q_y transition around 800 nm. Within every subunit, a Car protrudes between the α and β polypeptides, passing close to the BChls and enabling fast excitation energy transfer among the two types of cofactors. The Cars are in the all-*E* configuration and have a structural role connecting adjacent subunits; i.e., without Cars, the LH2 complexes fail to assemble (*24*).

In our study, the experimental secondary shifts of the LH2 *acidophila* complex determined by solid-state NMR are compared to chemical shifts predicted from the available X-ray structure (PDB entry 1NKZ) using SHIFTX. This program uses a semiempirical approach to estimate shifts for a given PDB structure from a database of NMR shifts for similar structures and sequences and calculates the side chain electrostatic, hydrogen bonding, and ring current contributions to the chemical shift (*8*). We find that the majority of residues exhibiting pronounced secondary shift anomalies are involved in pigment−protein or protein−protein contacts, and DFT shift calculations for several residues for which the experimental data and structure-based shift predictions diverge support the idea that the backbone chemical shifts are affected by the quaternary structure. Apparently, the secondary shifts are quite sensitive to higher-order contacts that induce atomic-level structural or electronic perturbations, to such an extent that for this densely packed complex a standard analysis can be applied to map out sites of local strain and electrostatic interactions. For photosynthetic antennae, it is well-known that protein-induced structural distortions and electronic perturbations of the cofactors affect and control the excited-state energies. Our analysis suggests that vice versa the protein matrix is also perturbed, giving a complementary view of functional molecular interactions that build up natural light-harvesting assemblies.

MATERIALS AND METHODS

The chemical shift assignment of the *Rps. acidophila* LH2α and LH2β polypeptides and experimental details have been described by van Gammeren et al. (*14*). Briefly, isotopically enriched [^{13}C,^{15}N]LH2 complexes were obtained by growing the photosynthetic purple bacteria *Rps. acidophila* 10050 anaerobically in light at 30 °C on a well-defined medium (*25*). For label incorporation, ^{13}C-labeled succinic acid was prepared by a multistep synthesis starting from ^{13}C-labeled acetic acid. The protein complex structural integrity after purification was verified by measurement of the UV−vis absorption spectrum that is characteristic of the LH2-bound chromophores. The purified LH2 complexes were solubilized in lauryl dimethyl amine oxide (LDAO) at detergent concentrations well above the critical micelle concentration (CMC). Two-dimensional (2D) homonuclear ^{13}C−^{13}C and heteronuclear ^{13}C−^{15}N correlation spectra were recorded by MAS NMR spectroscopy on a Bruker AV-750 spectrometer equipped with a two-channel CP-MAS probe head and with a ^{13}C radiofrequency of 188 MHz. All samples were cooled to 253 K, and the MAS spinning frequency was 8.5 kHz. Chemical shifts are referenced relative to 2,2-dimethyl-2-silapentane-5-sulfonic acid (DSS). Data were analyzed and compared with the PDB structure of the LH2 of *Rps. acidophila* (PDB entry 1NKZ) using SHIFTX (*8*).

DFT calculations of the C_a and C_b chemical shifts were performed in vacuo with the BLYP functional. Test calculations have shown that the use of the hybrid B3LYP functional does not affect significantly the results (*26*). Calculations of His in different protonation states were performed using the Gaussian 03 package (*27*) with the 6-311++G(d,p) basis set. All other DFT calculations were performed with the ADF code (*28*) and a TZP basis set. We have verified that the use of a different basis set does not change significantly the computed chemical shift differences (see also Table 1 of Results and Discussion). For the His−BChl calculation, the phytyl tail of the bacteriochlorophyll *a* was truncated at the esther group and saturated with a hydrogen atom in the model. This truncation has little effect on the electronic structure of the porphyrin ring. The NMR chemical shifts were calculated using the GIAO method, and the calculated ^{1}H and ^{13}C shieldings were referred to the tetramethylsilane (TMS) chemical shift.

RESULTS

α-Helical proteins are characterized by positive C_a chemical shifts compared to random coil (rc) values ($\delta C_a > 0$) and negative δC_b values. Alternatively, the chemical shifts can be combined in an offset independent manner, with secondary shifts defined as $\delta(C_a-C_b) = (C_a - C_{a[rc]}) - (C_b - C_{b[rc]})$. Figure 1 presents the experimental δC_a and δC_b shifts for the LH2α and LH2β polypeptides. In both panels A and B, the sequence is listed and the α-helical stretches according to the crystal structure are underlined. The arrows point toward residues in the transmembrane (TM) region that have secondary shifts deviating from α-helical, i.e., with negative δC_a or positive δC_b. For the LH2α polypeptide, these are residues αL20 and αI26 and the αW40−αW45 stretch. For the LH2β polypeptide, deviations occur for residues βE6, βQ7, βK13, βI16, βD17, βT19, and βF22. The absolute values for αY44 C_a, βQ7 C_a and C_b, and βK13 C_a are out of the statistical range, i.e., deviating more than 2σ from the statistical averages in the Biological Magnetic Resonance Bank (BMRB). Taken together, the secondary shifts fail to correctly predict the secondary structure in specific regions, hampering the use of programs like TALOS to predict the protein dihedral angles. The second α-helical stretch of the LH2α polypeptide is not reflected in the secondary shifts, and the first part of the α-helix of the LH2β polypeptide (up to residue 22) would be classified as random coil.

In a second step, we make the connection between the X-ray structure and the NMR data. We compared the experimental secondary chemical shifts with secondary shifts predicted

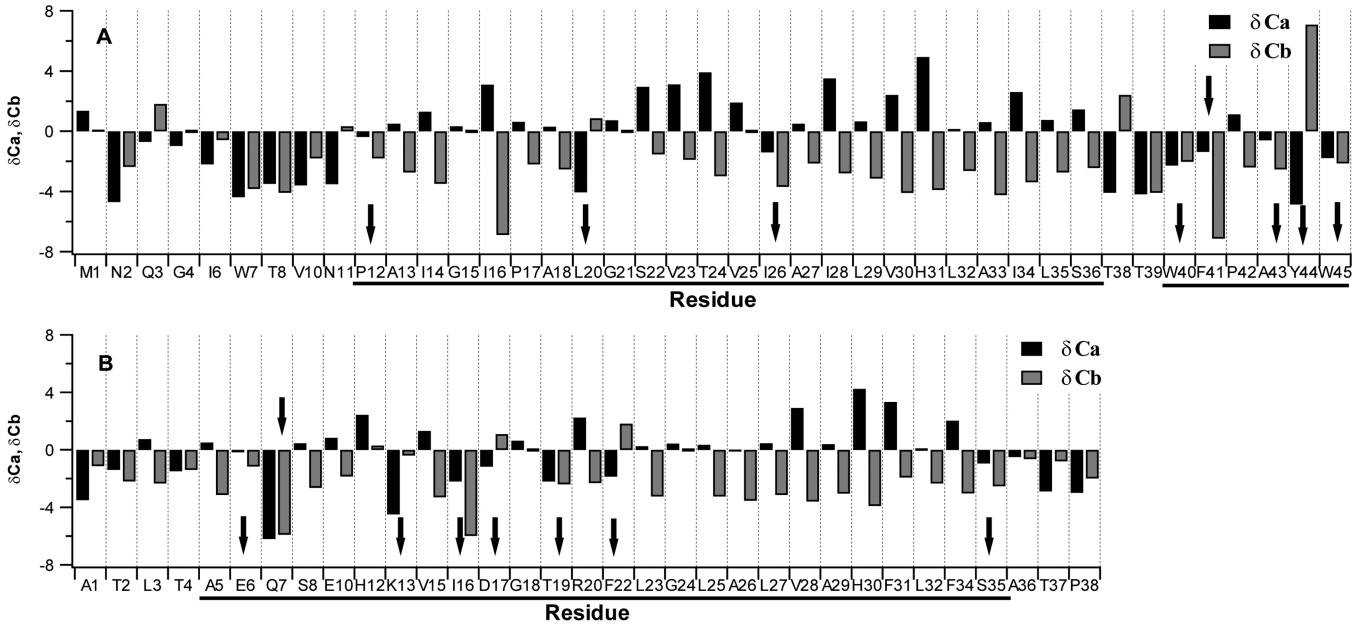

FIGURE 1: Experimental δC_a and δC_b secondary shifts of the LH2α (A) and LH2β (B) polypeptides. The α-helical parts of the protein sequences are underlined. Arrows point toward residues within the α-helical stretches for which the secondary shifts do not agree with an α-helical structure.

from the LH2 crystal structure (PDB entry 1NKZ) using SHIFTX (*8*). Figure 2 presents the differences $\{\delta_{SHIFTX\text{-}obs} = [\delta(C_a-C_b)]_{[SHIFTX]} - [\delta(C_a-C_b)]_{[observed]}\}$ between the secondary shifts predicted by SHIFTX and those observed by NMR, while Figure S1 of the Supporting Information shows the differences between the individual SHIFTX-calculated and the observed C_a, C_b, and CO chemical shifts. The secondary shifts deviate much more than the rmsd errors of 0.98, 1.10, and 1.16 ppm reported for C_a, C_b, and CO signals, respectively (*8*). Important secondary shift deviations ($|\delta_{SHIFTX\text{-}obs}| > 4$ ppm), well outside the rmsd range, are detected for αI6, αI116, αL20, αH31, and αY44 in the LH2α subunit and for βL3, βK13, βD17, βT19, βL23, and βH30 in the LH2β subunit. The Mg-coordinating αH31 and βH30 have experimental C_a and C_b chemical shifts that fulfill the criteria for α-helical secondary shifts ($\delta C_a > 0$ and $\delta C_b < 0$). However, the C_a atoms are ~2.5 ppm downfield compared to the corresponding SHIFTX estimates, and the C_b atoms are ~2 ppm upfield from the SHIFTX values, yielding large negative values for $\delta_{SHIFTX\text{-}obs}$. In addition to residues with large $\delta_{SHIFTX\text{-}obs}$ values, large shift deviations are observed for αF41, which has its C_a and C_b signals both downshifted by 5 and 3 ppm, respectively, compared to the SHIFTX estimates. Finally, pronounced deviations from the crystal structure-predicted CO chemical shifts occur for αI26, αT39, βQ7, and βR20 (Figure S1 of the Supporting Information).

Of the 70 residues on which the SHIFTX analysis was performed, 28 are involved in protein−protein or pigment−protein contacts according to the crystal structure of PDB entry 1NKZ. Both the contact and noncontact residues have secondary shifts that deviate more than the rms error of ~1 ppm that is quoted for the expected SHIFTX differences between the observed and calculated C_a and C_b shifts. Many of the residues with large secondary shift anomalies have side chains in contact with the B800 BChls (αL20, βT19, and βR20), with the B850 BChls (αI26, αH31, αF41, αY44, βL23, and βH30), or with the Cars (αI6, αL20, αI26, βT19, and αH31) or are involved in oligomerizing H-bond interactions (βL3, αT39, and αY44) (*22*, *29*). For residues with anomalous shifts that reside close to the BChl macrocycles, the distances between the C_a and C_b atoms and the BChl porphyrin rings were measured taking the crystal structure of PDB entry 1NKZ. The distances between the backbone atoms and the BChl macrocycles were > 5 Å except for that of βL23. This residue has its C_a atom within 4 Å of the BChl O17[4] atom and can experience small ring current effects (i.e., < 1 ppm) from the nearby BChl that are not included in the SHIFTX estimates. For the other residues, the possibility of ring current shifts induced by the BChl macrocycles and contributing to the secondary shift anomalies can be discarded.

To test if there is a significant correlation between structural motifs and the deviations between the experimental and SHIFTX-predicted secondary ($C_a - C_b$) shifts that are presented in Figure 2, we separated contact and noncontact residues. A χ^2 analysis gives an rmsd for the difference between experimental and SHIFTX-predicted shifts of 4.3 ppm for contact residues, versus 2.3 ppm for noncontact residues. Three of the 42 noncontact residues (7.1%) have secondary shifts with very large deviations (≥4 ppm) compared to their SHIFTX-predicted values, versus 7 of the 28 contact residues (25%). If we leave out the residues that have C_a and/or C_b values out of statistical range according to the BMRB, i.e., αY44, βQ7, and βK13, we obtain rms values of 3.4 ppm for contact residues versus 1.8 ppm for the noncontact residues, also well above the expected SHIFTX rms error of ~1 ppm (*8*). We emphasize that while most of the large shift anomalies occur for residues involved in pigment or protein contacts, not all of the important contact residues have anomalous secondary shifts.

DISCUSSION

According to the X-ray structure and functional investigations of the LH2 system, the majority of residues that have a large divergence between the NMR data and the SHIFTX calculations are involved in higher-order interactions stabilizing the complex and supporting its light-harvesting function (*26*, *29*−*31*). By mapping the large anomalous secondary shifts (i.e., with $|\delta_{SHIFTX\text{-}obs}| >$ 4 ppm and/or individual C_a, C_b, or CO shifts deviating more than

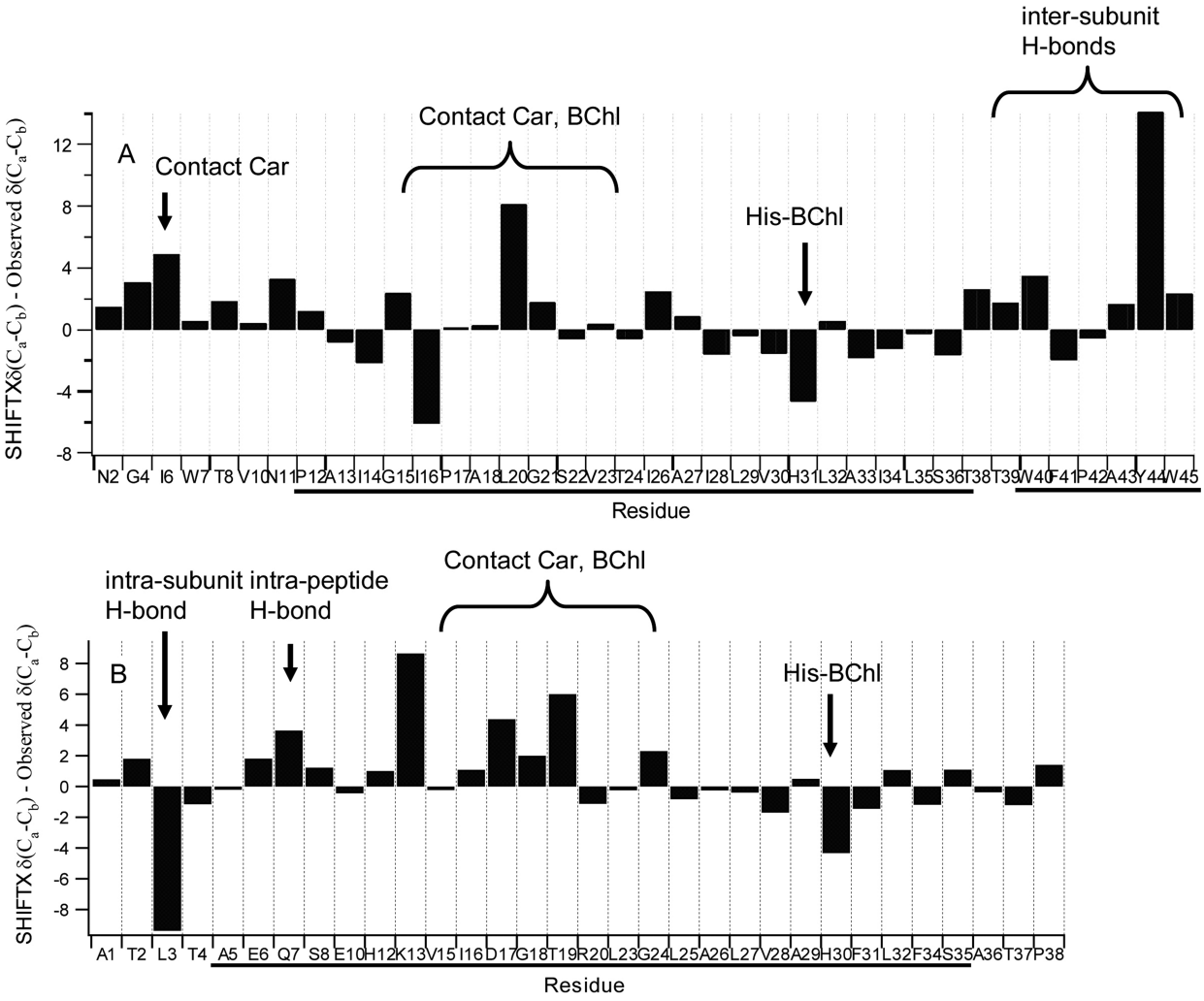

FIGURE 2: Difference shifts between the experimentally observed and SHIFTX-predicted secondary shifts defined as $\delta_{\text{SHIFTX-obs}} = [\delta(C_a-C_b)]_{\text{SHIFTX}} - [\delta(C_a-C_b)]_{\text{observed}}$ for the (A) LH2α and (B) LH2β polypeptides. The α-helical parts of the protein sequences are underlined. Cofactor−protein or protein−protein contacts coincide with anomalous shift regions.

4 ppm from their SHIFTX estimates) on the LH2 structure in Figure 3, we can distinguish different protein regions. The first region is near the N-terminal part, including anomalous secondary shifts for βL3 and βQ7 that stabilize the $\alpha\beta$ subunit and the peptide tertiary structure, respectively. The second region is around the B800 BChl-binding region, where both BChls and Cars are in van der Waals contact with the protein. The third region is around the B850 BChl binding region and contains the coordinating histidines, and the fourth region is near the B850 band at the second LH2α α-helical stretch, containing residues αT39, αF41, and αY44. We propose that the complex stabilizing interactions can lead to anomalous shifts if they include local strain or unusual electrostatic effects and discuss these interactions below in more detail.

B850 Region: The BChl-Coordinating Histidines. For the BChl-coordinating histidines (His) in LH2, detailed information about the side chains has already been obtained by MAS NMR experiments on isotope-labeled His in this complex in combination with DFT calculations (*32*, *33*). It was found that the protein environment stabilizes the His side chain very close to the B850 BChl Mg ion, inducing a significant bond length deformation in the His imidazole ring. This leads to an electronic structure and shifts similar to those of imidazolium and an induced electronic charge transfer of ~0.5 electronic equivalent of charge stabilized on the ring (*26*). In the B850 dimer, the overlapping macrocycles of the B850 BChl pairs in each subunit are stabilized by the curvature of the LH2 ring. Because the protein complex is rigid, it can exert a counterforce, by making an unfavorable angle with the main chain or by residing close to the BChl. This explains why DFT calculations on His−BChl models can reproduce only the experimentally derived His side chain chemical shifts in single-point calculations with geometries taken directly from the LH2 crystal structure (*26*).

We applied DFT calculations to explore the relation between the backbone chemical shift deviations and side chain His−BChl interactions. The BChl-coordinating αHis31 and βHis30 residues are formally in a neutral$_\pi$ state, also known as N_3 tautomers, i.e., with the imidazole nitrogen protonated at the π position near the C_γ atom, while the other nitrogen is coordinated to the BChl Mg. However, the coordinating His residues have side chain chemical shifts corresponding to a double-protonated or positive state, i.e., with both the imidazole nitrogens protonated, due to the BChl−His electronic charge transfer effect. We tested (1) how the BChl coordination and concomitant charge transfer affect the His C_a and C_b shifts, by comparing DFT calculations of αH31 coordinated to BChl *a* to the αH31 structure without BChl in a neutral$_\pi$ state, and (2) how His protonation states affect the backbone shifts by comparing DFT calculations on His in a neutral$_\pi$, neutral$_\tau$ (also known as the N_1 tautomer with the

Table 1: DFT-Calculated Chemical Shifts for Different Types of His[a]

atom	N_τ	N_π	His+	αH31···Mg BChl	αH31	αH31 experiment
C_a	63.2 (63.4)	64.8	64.6 (64.9)	63.8	65.9	60.7
C_b	42.5 (41.4)	34.3	37.2 (36.4)	31.5	34.2	25.6

[a]The C_a and C_b chemical shifts (parts per million) of histidine in three protonation states, i.e., neutral$_\tau$ (N_τ), neutral$_\pi$ (N_π), and positively charged His (His+), calculated by DFT/BLYP using the Gaussian 6-311++G(d,p) basis set and of αH31 taken directly from the crystal structure of PDB entry 1NKZ with and without its coordinated BChl (i.e., N_π His) calculated with ADF. The last column presents the experimental shifts referenced to TMS. In parentheses are the values obtained by DFT/BLYP using the TZP basis set of ADF for comparison.

imidazole nitrogen at the τ position next to the C_δ protonated), and double-protonated state. The results are listed in Table 1. Since the calculations depend on the basis set that was used, we show in parentheses the values obtained by DFT/BLYP using the TZP basis set of ADF for the sake of comparison. The His-(−BChl) structures were taken directly from the crystal structure of PDB entry 1NKZ, and single-point calculations were performed. For all our DFT calculations, the chemical shift values consistently have a large offset compared to the experimental shift values. We therefore cannot compare the absolute values of the calculations to the NMR experiment but focus on the $C_a - C_b$ difference values. The largest DFT calculated $C_a - C_b$ difference value (32.3 ppm) is found for αH31 coordinated to BChl, which is closest to the experimental difference shift of 35.1 ppm. The calculations show that the coordinating BChl induces a −2.1 ppm upfield shift of the C_a and −2.7 ppm upfield shift of the C_b responses, showing that the His···BChl coordination and concomitant charge transfer indeed have a significant effect on the backbone chemical shifts. The His protonation state has an even more pronounced effect on the C_b responses, with an ∼8 ppm difference between N_τ and N_π His. The effects of BChl coordination and His protonation states are not taken into account in the SHIFTX analysis, where the C_a and C_b shift estimates for βH12, for a His in a neutral$_\tau$ state, and for the BChl-coordinating αH31 and βH30 differ by only 0.6−1.1 ppm. The DFT calculations thus reveal that the His protonation states, BChl coordination, and associated electronic structures propagate into the backbone and affect the secondary chemical shifts, an effect which is not included in the empirically derived SHIFTX values.

B850 Region: αT39, αF41, and αY44. The largest chemical shift anomalies are observed for the C_a and C_b chemical shifts of αY44, a residue that is important both for stabilizing the LH2 ring structure and for tuning the color of the B850 BChls. Both the αY44 and αW45 side chains are involved in hydrogen bonding to a B850 BChl, but while the αW45 forms an intrasubunit hydrogen bond, αY44 is hydrogen-bonded to the βB850 BChl C3 acetyl chain of the preceding subunit, stabilizing the LH2 ring by connecting adjacent subunits (*22*, *29*). Replacement of αY44 with leucine LH3 complexes grown under low-light conditions results in a 30 nm blue shift of these complexes, of which part is believed to originate from a more pronounced out-of-plane rotation of the BChl C3-acetyl (*31*). The threonine αT39 has C_a and CO chemical shifts that are more than 4 ppm upfield from the SHIFTX predictions. This residue, like αY44, connects adjacent subunits in a ring, by hydrogen bonding to αQ46 of the proceeding α-polypeptide. The phenylalanine αF41

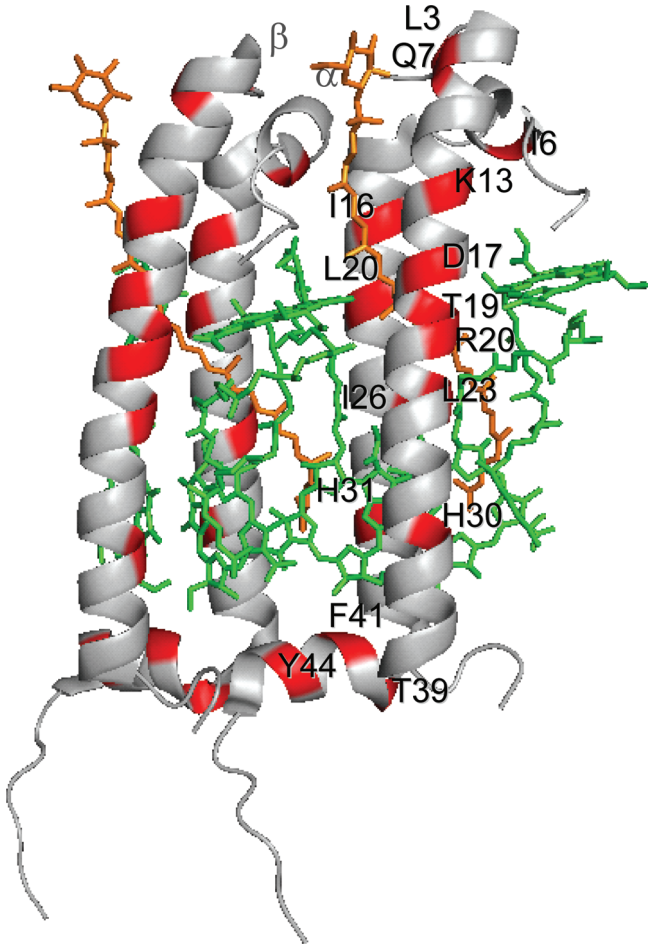

FIGURE 3: Structure of the LH2 *Rps. acidophila* complex with two $\alpha\beta$ subunits, highlighting the residues with large secondary shift anomalies. BChls are colored green, and Car is colored orange. The highlighted residues are labeled for the $\alpha\beta$ subunit on the right side. Highlighted residues have experimental secondary shifts deviating more than 4 ppm from the SHIFTX-estimated values ($|\delta_{SHIFTX\text{-}obs}| \geq 4$ ppm) and/or large individual δCO, δC_a, or δC_b chemical shift displacements ($|\delta X{=}O|$, $|\delta C_a|$, or $|\delta C_b| \geq 4$ ppm).

has both significant upfield-shifted C_a (3 ppm) and C_b (5 ppm) chemical shifts compared to the SHIFTX-predicted values. The residue is located within van der Waals distance of the αB850 BChl and between residues T39 and Y44 that connect to proceeding and preceding subunits, respectively. In the structure of PDB entry 1NKZ, the αF41 C_b-C_a-C and C_a-C-N bond angles are larger than average, exceeding three standard deviations (SD), suggesting that this residue is in a restrained conformation.

B800 Region. Compared to the B850 binding region with few selective perturbed secondary shifts, the B800 binding region, where the B800 BChls, B850 phytyl chains, and Car have to fit in the complex, has a larger area of perturbed shifts. In the LH2 complex of *Rps. acidophila*, the Cars are twisted due to the restrained pigment−protein contacts, and they will reversibly induce pressure on the protein around the B800 region where van der Waals contacts occur. In the same region, the protein has to accommodate the B800 BChl macrocycles that are oriented perpendicular to the transmembrane α-helices. In addition to protein−cofactor interactions, the dipoles formed by the intra-helix ion pairs between βK13 and βE10 and between βD17 and βR20 probably contribute to the observed secondary shift displacements for βK13 and βD17.

Table 2: Release of Energy upon Structural Relaxation of Nine-Residue Peptide Fragments

target residue	ΔE^a (kcal/mol)
βQ7	−14.2 (21 atoms)
βD17	−18.7 (16 atoms)
αT24	−6.7 (18 atoms)
αH31	−13.1 (23 atoms)
αF41	−9.1 (22 atoms)

[a]DFT-calculated energy differences between target residues taken directly from the crystal structure of PDB entry 1NKZ and taken from nine-residue fragments that were structurally relaxed by performing a geometry optimization.

N-Terminal Region. In the N-terminal region, two deviating secondary shifts are observed for the LH2β polypeptide. βQ7 interacts with βT4, with hydrogen bonds between the βQ7 side chains and the βT4 main chain and vice versa, stabilizing the tertiary structure that changes from an amphipathic stretch at the N-terminal side to a transmembrane helical stretch. βL3 is hydrogen-bonded to αW7, stabilizing the αβ subunit.

Molecular-Mechanics Geometry Optimization Procedure of Polypeptide Fragments. To determine if the secondary shift anomalies were induced by locally restrained backbone conformations, induced by higher-order interactions, one target residue of each region that displayed anomalous secondary shifts (βQ7, βD17, αH31, and αF41) was taken and subjected to a molecular-mechanics (MM) geometry optimization procedure. As a control, the procedures were also performed for a residue without deviating secondary shifts (αT24). In the procedure, a nine-residue fragment with the target residue centered at position 5 was taken from the LH2 crystal structure of PDB entry 1NKZ. The lengths of the fragments were chosen as the minimal lengths that allow the formation of helix-stabilizing H-bonds between the target residue NH group and the carbonyl of the preceding $i - 4$th residue, as well as between the carbonyl of the target residue and the NH group of the proceeding $i + 4$th residue, to maintain the secondary structural effects. The two outer residues at position 1 and 9 were fixed, while the seven inner residues, including the target one, were geometry optimized using the Amber force field. The target residue was further optimized quantum mechanically. The energy releases upon structural relaxation are presented in Table 2. They are indeed larger for the residues with secondary shift anomalies compared to the control case, in line with the occurrence of local strain. Typical coordinate rms displacement of the target residue after relaxation was on the order of 0.5 Å, and the optimization procedure involved changes of ∼5° in the backbone N−C−C_a−C_b and N−C_a−C_b−C_γ torsion angles. Comparable rms coordinate changes of ∼0.2 Å and ∼5° in rms backbone dihedral angles have been described for pressure-dependent protein structural changes, based on ^{1}H chemical shifts (*34*). After structural relaxation of the αF41 fragment, its C_b−C_a−C and C_a−C−N bond angles, which have out-of-range values in the crystal structure, fell within the range of average values.

The C_a and C_b chemical shifts were calculated for the target residues taken directly from the crystal structure (single-point calculations) and after structural relaxation of the peptide fragments. Also, here the DFT-calculated shifts have an offset compared to the experimental shifts, and only the C_a−C_b difference shifts can be compared to the experimental values. We supposed that the single-point calculations on the crystal structure fragments would give more realistic values; however, for βQ7 and βD17, the C_a−C_b shifts calculated for the structurally relaxed fragments are in much better agreement with the experimental difference shifts (Table S1 of the Supporting Information). No clear trend is visible between strain released upon relaxation (ΔE in Table 2) and the magnitude of the chemical shift changes upon relaxation, and similar shifts of ∼3 ppm are predicted for the control residue. The single-point calculations were run on X-ray structures without any optimization of atom bond lengths and angles, and they may contain the effects of small random bond length or angle errors in the crystal structure. Such errors are removed after running a geometry optimization. This may explain the substantial shift changes that are predicted for the control residue and suggests that our approach relating chemical shifts to local strain effects is limited by the resolution of the crystal structure. Only αF41 clearly has distorted dihedral angles in the X-ray structure, of which we could confirm that the distortive features are removed upon structural relaxation. We expect that the observed shifts include the effect of the specific distortion, whereas it is not taken into account in the SHIFTX predictions that rely on the comparison with databases of proteins with common torsion angles. The difference between the single-point and geometry-optimized calculated shifts indeed follows the trend between the experimental shifts and the SHIFTX estimates, i.e., −8.2 and −7.6 ppm for calculated C_a and C_b differences before and after relaxation, respectively (Table S1 of the Supporting Information), compared to a $\delta C_{a[OBS\text{-}SHIFTX]}$ of −3 ppm and a $\delta C_{b[OBS\text{-}SHIFTX]}$ of −5 ppm for the differences between the observed and SHIFTX-predicted shifts. In addition to backbone restraints and side chain electrostatic interactions, the long-range electrostatic field of the cofactors could contribute to the secondary shift perturbations, especially around the B800 band. To describe fully the factors that affect the secondary shifts, also these electrostatic field effects should be integrated into the DFT calculations, for instance, using a frozen-density embedding method, a subsystem approach to DFT (*35*).

In summary, anomalous secondary shifts appearing in the LH2 antenna complex are observed for residues involved in stabilizing (i) H-bonding intrapeptide (βQ7), intrasubunit (αL3), and intersubunit (αT39 and αY44) interactions, (ii) intrahelix ion pair interactions (βK13 and βD17), (iii) van der Waals protein−cofactor interactions, and (iv) ligand-coordinating interactions (αH31 and βH30). Perturbations of the secondary shifts occur apparently through side chain interactions, as shown for the BChl-coordinating His, or through backbone deformations, as proposed for αF41, and can involve both peptide−peptide and peptide−cofactor interactions. On the atomic level, structural and electrostatic perturbations are interconnected and can induce small displacements of the C_a and C_b spin nuclei that give rise to chemical shift anomalies. The earlier described His−BChl charge transfer effect is an example, where the packing of the pigments and polypeptides in the oligomeric complex leads to electronic charge transfer between the His and the coordinating BChl, and corresponding bond length alterations of the His imidazoles. Also, for the backbone chemical shifts, electronic perturbations by definition cannot always be separated from structural perturbations.

Due to the high local sensitivity of the NMR chemical shifts, small structural perturbations might be detected as anomalous shifts, even if the backbone bond lengths and angles are not outside the range in the X-ray structure. On the other hand,

there are many (predominantly side chain) protein−protein and pigment−protein interactions in the crystal structure, which do not induce significant electronic or structural perturbations that propagate into the backbone. It is likely that chemical shift anomalies occur only for these interactions that involve strong or unusual electrostatic effects or that induce local deformations of the backbone dihedral angles. Such interactions will be more abundant in rigid, pigment-containing, and oligomeric complexes than in soluble, flexible proteins and could explain why the rms difference between observed and SHIFTX-predicted shifts for the LH2 protein is larger than the quoted value for this method.

Implications for Structure and Function. Our finding of distinctive regions of anomalous shifts around the B850 and B800 bands is in agreement with high-pressure studies on LH2 complexes that suggest that the LH2 protein has two independent structural domains (*36*). The first domain around the B850 band is pressure-independent for hydrostatic pressures up to 0.6 GPa but shows significant alterations of the tertiary structure at higher pressures, including breakage of hydrogen bonds (*37*), while the second domain around the B800 band is already perturbed at lower pressures, causing the loss of the B800 BChls. We report that the B800 region is characterized by many secondary shift perturbations around van der Waals protein−pigment contacts, while the B850 region is characterized by few perturbed residues that connect to the B850 BChls and are involved in H-bonds stabilizing the ring-shaped assembly. In addition, two areas within the B850 domain are distinguished: the α and β BChl-coordinating His and the second helical part of LH2α.

In flexible proteins, the amino acid side chains can form multiple interchangeable nonbonded interaction networks, corresponding to iso-energetic minima in the energy landscape. Under these competing conditions, the system is frustrated. Enzymatic proteins often display locally frustrated areas around ligand binding sites that are stabilized upon complexation, by reducing the exposure of the protein surface to the water environment. This phenomenon is described in terms of an induced fit, referring to a conformational change in the protein upon ligand binding, leading to local optimization of the binding pocket (*38*). In contrast, for the transmembrane LH2 complex, a very stable fold is observed that is overall weakly frustrated because it contains a well-defined and settled network of stabilizing nonbonded interactions. Here apparently complexation of pigments and polypeptides creates "induced misfits", local distortions that are established by the packing of the polypeptides and pigments into a complex and that are the energetic costs of an overall tight folding and energetically favorable oligomerization reaction. The concept of an induced misfit was introduced recently in the context of ligand receptor interactions in the rhodopsin visual G-protein-coupled receptor, where an improper fit of a non-native 9-*cis*-retinylidene ligand was observed via MAS NMR (*39*).

Interpreting the secondary shift anomalies in terms of local strain, we can speculate about the functionality. For photosynthetic antenna proteins, nuclear motions affect the pigment electronic transition energies, causing dynamic and static disorder that is manifested as homogeneous and inhomogeneous broadening of optical spectra (*40*). Fast dynamics on the scale of the fluorescent lifetime leads to dynamic disorder and involves molecular vibrations and effective exciton−phonon coupling (*41*). In the TLS (translation, libration, screw) refinement of the LH2 *Rps. acidophila* crystal structure, molecular displacements connected to functionally relevant motions were identified (*22*) and localized strain is a liable source for such nonrandom displacements, which, according to its calculated associated energy changes, can provide a significant contribution to functional interpigment interactions between the B850 BChls. The associated slow dynamics give rise to a better functional absorption profile by static broadening on the short time scale of optical absorption, in a structural environment that is very homogeneous. The structural displacements may involve very minor His−Mg bond length alterations that are averaged on the long time scale of the NMR. For LH2 complexes, the dynamic trajectories of the slow dynamics have been monitored as room-temperature fluctuations in single-molecule fluorescence spectra, and spectral jumps were explained by the existence of "quasi-stable" states (*42*). Local points of strain in the LH2 backbone will lower the energy barriers to switch between such states and predict the sites in the protein conformational fluctuations that are likely to appear.

CONCLUDING REMARKS

The high density of pigments and the rigid character of the LH2 antenna complex produce both structural and electronic local perturbations that have not yet been observed to a similar extent in other membrane proteins. Standard secondary shift analyses inherently do not take into account higher-order folding properties, which are often established through side chain contacts. The finding of anomalous backbone shifts in such analysis can be a first indication of specific higher-order interactions, without the necessity of assigning the involved side chain atoms. In particular, for photosynthetic complexes, which are relatively rigid protein structures that are abundant in chromophores, the standard analyses could be exploited to obtain information about localized conformational strain and electrostatic pigment−protein interactions, complementary to crystallographic data. By mapping the anomalous NMR secondary shifts on to the protein structure, we have now an overview of atomic-level backbone perturbations for the two types of polypeptides that build up the LH2 ring, providing unique information about the electronic structure and the underlying tensions in the conformational structure of a large, oligomeric pigment−protein complex.

SUPPORTING INFORMATION AVAILABLE

C_a, C_b, and CO chemical shift differences between the experimental NMR data and the SHIFTX estimates and absolute NMR chemical shift values for residues βQ7, βD17, αT24, αH31, and αF41 from DFT single-point calculations and from DFT calculations after a geometry optimization of nine-residue fragments. This material is available free of charge via the Internet at http://pubs.acs.org.

REFERENCES

1. Wishart, D. S., Sykes, B. D., and Richards, F. M. (1991) Relationship between nuclear magnetic resonance chemical shift and protein secondary structure. *J. Mol. Biol. 222*, 311–333.
2. Iwadate, M., Asakura, T., and Williamson, M. P. (1999) Ca and Cb carbon-13 chemical shifts in proteins from an empirical database. *J. Biomol. NMR 13*, 199–211.
3. Castellani, F., van Rossum, B., Diehl, A., Schubert, M., Rehbein, K., and Oschkinat, H. (2002) Structure of a protein determined by solid-state magic-angle-spinning NMR spectroscopy . *Nature 420*, 98–102.
4. Herzfeld, J., and Berger, A. E. (1980) Sideband intensities in NMR spectra of samples spinning at the magic angle. *J. Chem. Phys. 73*, 6021–6030.
5. Wylie, B. J., Franks, T., and Rinestra, C. M. (2006) Determinations of ^{15}N Chemical Shift Anisotropy Magnitudes in a Uniformly ^{15}N,^{13}C-Labeled Microcrystalline Protein by Three-Dimensional

Magic-Angle Spinning Nuclear Magnetic Resonance Spectroscopy. *J. Phys. Chem. B 110*, 10926–10936.
6. Wylie, B. J., Sperling, L. J., Frericks, H. L., Shah, G. J., Franks, W. T., and Rienstra, C. M. (2007) Chemical-shift anisotropy measurements of amide and carbonyl resonances in a microcrystalline protein with slow magic-angle spinning NMR spectroscopy. *J. Am. Chem. Soc. 129*, 5318–5319.
7. Ganapathy, S., van Gammeren, A. J., Hulsbergen, F. B., and de Groot, H. J. M. (2007) Probing secondary, tertiary, and quaternary structure along with protein-cofactor interactions for a helical transmembrane protein complex through H-1 spin diffusion with MAS NMR spectroscopy. *J. Am. Chem. Soc. 129*, 1504–1505.
8. Neal, S., Nip, A. M., Zhang, H. Y., and Wishart, D. S. (2003) Rapid and accurate calculation of protein H-1, C-13 and N-15 chemical shifts. *J. Biomol. NMR 26*, 215–240.
9. Kijac, A. Z., Li, Y., Sligar, S. G., and Rienstra, C. M. (2007) Magic-angle spinning solid-state NMR spectroscopy of nanodisc-embedded human CYP3A4. *Biochemistry 46*, 13696–136703.
10. Heise, H., Luca, S., de Groot, B. L., Grubmüller, H., and Baldus, M. (2005) Probing conformational disorder in neurotensin by two-dimensional solid-state NMR and comparison to molecular dynamics simulations. *Biophys. J. 89*, 2113–2120.
11. Shen, Y., Lange, O., Delaglio, F., Rossi, P., Aramini, J. M., Liu, G., Eletsky, A., Wu, Y., Singarapu, K. K., Lemak, A., Ignatchenko, A., Arrowsmith, C. H., Szyperski, T., Montelione, G. T., Baker, D., and Bax, A. (2008) Consistent blind protein structure generation from NMR chemical shift data. *Proc. Natl. Acad. Sci. U.S.A. 105*, 4685–4690.
12. Vila, J. A., Aramini, J. M., Rossi, P., Kuzin, A., Su, M., Seetharaman, J., Xiao, R., Tong, L., Montelione, G. T., and Scheraga, H. A. (2008) Quantum chemical ^{13}C chemical shift calculations for protein NMR structure determination, refinement, and validation. *Proc. Natl. Acad. Sci. U.S.A. 105*, 14389–14394.
13. Egorova-Zachernyuk, T. A., Hollander, J. G., Fraser, N. J., Gast, P., Hoff, A. J., Cogdell, R. J., de Groot, H. J. M., and Baldus, M. (2001) MAS NMR on a uniformly ^{13}C,^{15}N labeled LH2 lightharvesting complex from Rhodopseudomonas acidophila 10050 at ultra-high magnetic fields. In Focus on Structural Biology , Kluwer Academic Publishers, Dordrecht, The Netherlands.
14. van Gammeren, A. J., Hulsbergen, F. B., Hollander, J. G., and de Groot, H. J. M. (2005) Residual backbone and side-chain C-13 and N-15 resonance assignments of the intrinsic transmembrane light-harvesting 2 protein complex by solid-state Magic Angle Spinning NMR spectroscopy. *J. Biomol. NMR 31*, 279–293.
15. Cornilescu, G., Delaglio, F., and Bax, A. (1999) Protein backbone angle restraints from searching a database for chemical shift and sequence homology. *J. Biomol. NMR 13*, 289–302.
16. Cogdell, R. J., Gall, A., and Kohler, J. (2006) The architecture and function of the light-harvesting apparatus of purple bacteria: From single molecules to in vivo membranes. *Q. Rev. Biophys. 39*, 227–324.
17. Parkes-Loach, P. S., Sprinkle, J. R., and Loach, P. A. (1988) Reconstitution of the B873 light-harvesting complex of *Rhodospirillum rubrum* from the separately isolated α-polypeptide and *β*-polypeptide and bacteriochlorophyll a. *Biochemistry 27*, 2718–2727.
18. Pandit, A., Visschers, R. W., van Stokkum, I. H. M., Kraayenhof, R., and van Grondelle, R. (2001) Oligomerization of light-harvesting I antenna peptides of *Rhodospirillum rubrum*. *Biochemistry 40*, 12913–12924.
19. Pandit, A., van Stokkum, I. H. M., Georgakopoulou, S., van der Zwan, G., and van Grondelle, R. (2003) Investigations of intermediates appearing in the reassociation of the light-harvesting I complex of *Rhodospirillum rubrum*. *Photosynth. Res. 75*, 235–248.
20. Reynolds, N. P., Janusz, S., Escalante-Marun, M., Timney, J., Ducker, R. E., Olsen, J. D., Otto, C., Subramaniam, V., Leggett, G. J., and Hunter, C. N. (2007) Directed formation of micro- and nanoscale patterns of functional light-harvesting LH2 complexes. *J. Am. Chem. Soc. 129*, 14625–14631.
21. Suemori, Y., Nagata, M., Nakamura, Y., Nakagawa, K., Okuda, A., Inagaki, J. I., Shinohara, K., Ogawa, M., Iida, K., Dewa, T., Yamashita, K., Gardiner, A. T., Cogdell, R. J., and Nango, M. (2007) Self-assembled monolayer of light-harvesting core complexes of photosynthetic bacteria on an amino-terminated ITO electrode. *Photosynth. Res. 90*, 17–21.
22. Papiz, M. Z., Prince, S. M., Howard, T., Cogdell, R. J., and Isaacs, N. W. (2003) The structure and thermal motion of the B800−850 LH2 complex from *Rps. acidophila* at 2.0 Å resolution and 100 K: New structural features and functionally relevant motions. *J. Mol. Biol. 326*, 1523–1538.
23. Sundstrom, V., Pullerits, T., and van Grondelle, R. (1999) Photosynthetic light-harvesting: Reconciling dynamics and structure of purple bacterial LH2 reveals function of photosynthetic unit. *J. Phys. Chem. B 103*, 2327–2346.
24. Lang, H. P., and Hunter, C. N. (1994) The Relationship between Carotenoid Biosynthesis and the Assembly of the Light-Harvesting Lh2 Complex in *Rhodobacter sphaeroides*. *Biochem. J. 298*, 197–205.
25. Egorova-Zachernyuk, T. A., Hollander, J. G., Fraser, N. J., Gast, P., Hoff, A. J., Cogdell, R. J., de Groot, H. J. M., and Baldus, M. (2001) Heteronuclear 2D-correlations in a uniformly [^{13}C,^{15}N] labeled membrane-protein complex at ultra-high magnetic fields. *J. Biomol. NMR 19*, 243–253.
26. Wawrzyniak, P. K., Alia, A., Schaap, R. G., Heemskerk, M. M., de Groot, H. J. M., and Buda, F. (2008) Protein-induced geometric constraints and charge transfer in bacteriochlorophyll-histidine complexes in LH2. *Phys. Chem. Chem. Phys. 10*, 6971–6978.
27. Frisch, M. J., Trucks, G. W., Schlegel, H. B., Scuseria, G. E., Robb, M. A., Cheeseman, J. R., Montgomery, J. A., Vreven, J. T., Kudin, K. N., Burant, J. C., Millam, J. M., Lyengar, S. S., Tomasi, J., Barone, V., Mennucci, B., Cossi, M., Scalmani, G., Rega, N., Petersson, G. A., Nakatsuji, H., Hada, M., Ehara, M., Toyota, K., Fukuda, R., Hasegawa, J., Ishida, M., Nakajima, T., Honda, Y., Kitao, O., Nakai, H., Klene, M., Li, X., Knox, J. E., Hratchian, H. P., Cross, J. B., Adamo, C., Jaramillo, J., Gomperts, R., Stratmann, R. E., Yazyev, O., Austin, A. J., Cammi, R., Pomelli, C., Ochterski, J. W., Ayala, P. Y., Morokuma, K., Voth, G. A., Salvador, P., Dannenberg, J. J., Zakrzewski, V. G., Dapprich, S., Daniels, A. D., Strain, M. C., Farkas, O., Malick, D. K., Rabuck, A. D., Raghavachari, K., Foresman, J. B., Ortiz, J. V., Cui, Q., Baboul, A. G., Clifford, S., Cioslowski, J., Stefanov, B. B., Liu, G., Liashenko, A., Piskorz, P., Komaromi, I., Martin, R. L., Fox, D. J., Keith, T., Al-Laham, M. A., Peng, C. Y., Nanayakkara, A., Challacombe, M., Gill, P. M. W., Johnson, B., Chen, W., Wong, M. W., Gonzalez, C., and Pople, J. A. (2004) Gaussian 03 , revision C.02, Gaussian, Inc., Wallingford CT.
28. ADF2007.01, SCM, Theoretical Chemistry, Vrije Universiteit, Amsterdam, The Netherlands, http://www.scm.com.
29. Prince, S. M., Papiz, M. Z., Freer, A. A., McDermott, G., Hawthornthwaite-Lawless, A. M., Cogdell, R. J., and Isaacs, N. W. (1997) Apoprotein structure in the LH2 complex from *Rhodopseudomonas acidophila* strain 10050: Modular assembly and protein pigment interactions. *J. Mol. Biol. 268*, 412–423.
30. McDermott, G., Prince, S. M., Freer, A. A., Hawthornthwaite-Lawless, A. M., Papiz, M. Z., Cogdell, R. J., and Isaacs, N. W. (1995) Crystal Structure of an Integral Membrane Light-Harvesting Complex from Photosynthetic Bacteria. *Nature 374*, 517–521.
31. McLuskey, K., Prince, S. M., Cogdell, R. J., and Isaacs, N. W. (2001) The crystallographic structure of the B800−820 LH3 light-harvesting complex from the purple bacteria *Rhodopseudomonas acidophila* strain 7050. *Biochemistry 40*, 8783–8789.
32. Alia, Matysik, J., de Boer, I., Gast, P., van Gorkom, H. J., and de Groot, H. J. M. (2004) Heteronuclear 2D (H-1-C-13) MAS NMR resolves the electronic structure of coordinated histidines in light-harvesting complex II: Assessment of charge transfer and electronic delocalization effect. *J. Biomolecular NMR 28*, 157–164.
33. Alia, Matysik, J., Soede-Huijbregts, C., Baldus, M., Raap, J., Lugtenburg, J., Gast, P., van Gorkom, H. J., Hoff, A. J., and de Groot, H. J. M. (2001) Ultrahigh field MAS NMR dipolar correlation spectroscopy of the histidine residues in light-harvesting complex II from photosynthetic bacteria reveals partial internal charge transfer in the B850/His complex. *J. Am. Chem. Soc. 123*, 4803–4809.
34. Wilton, D. J., Kitahara, R., Kazuyuki, A., and Williamson, M. P. (2009) Pressure-dependent ^{13}C chemical shifts in proteins: Origins and applications. *J. Biomol. NMR 44*, 25–33.
35. Jacob, C. R., and Visscher, L. (2006) Calculation of nuclear magnetic resonance shieldings using frozen-density embedding. *J. Chem. Phys. 125*, 194104.
36. Gall, A., Ellervee, A., Sturgis, J. N., Fraser, N. J., Cogdell, R. J., Freiberg, A., and Robert, B. (2003) Membrane Protein Stability: High pressure Effects on the Structure and Chromophore-Binding Properties of the Light-Harvesting Complex LH2. *Biochemistry 42*, 13019–13026.
37. Kangur, L., Timpmann, K., and Freiberg, A. (2008) Membrane Protein Stability: High Pressure Effects on the Structure and Chromophore-Binding Properties of the Light-Harvesting Complex LH2. *J. Phys. Chem. B 112*, 7948–7955.
38. Koshland, D. E. (1958) Application of a Theory of Enzyme Specificity to Protein Synthesis. *Proc. Natl. Acad. Sci. U.S.A. 44*, 98–104.

39. Creemers, A. F. L., Bovee-Geurts, P. H. M., DeGrip, W. J., Lugtenburg, J., and de Groot, H. J. M. (2004) Solid-State NMR Analysis of Ligand-Receptor Interactions Reveals an Induced Misfit in the Binding Site of Isorhodopsin. *Biochemistry 43*, 16011–16018.
40. Novoderezkhin, V., Rutkauskas, D., and van Grondelle, R. (2006) Dynamics of the emission spectrum of a single LH2 complex: Interplay of slow and fast nuclear motions. *Biophys. J. 90*, 2890–2902.
41. van Grondelle, R., and Novoderezhkin, V. I. (2006) Energy transfer in photosynthesis: Experimental insights and quantitative models. *Phys. Chem. Chem. Phys. 8*, 793–807.
42. Rutkauskas, D., Olsen, J. D., Gall, A., Cogdell, R. J., Hunter, C. N., and van Grondelle, R. (2006) Comparative study of spectral flexibilities of bacterial light-harvesting complexes: Structural implications. *Biophys. J. 90*, 2463–2474.